Elastohydrodynamics of a pre-stretched finite elastic sheet lubricated by a thin viscous film with application to microfluidic soft actuators: supplementary material

Evgeniy Boyko, Ran Eshel, Khaled Gommed, Amir D. Gat and Moran Bercovici

Faculty of Mechanical Engineering, Technion – Israel Institute of Technology, Haifa, Israel

CONTENTS

A. Experimental methods

1. *Fabrication and device*

We fabricated our device using three-mask photolithography processes on top of a 100 mm diameter Borofloat wafer. We first deposited three parallel electrodes at a distance of 5 mm apart, using electron-beam physical vapor deposition. Outer electrodes are connected to a single contact pad, whereas the inner electrode is connected to a separate pad. The electrodes are composed of four layers - 300 Å titanium, 1000 Å platinum, 200 Å titanium, 1000 Å nickel, with the last layer (nickel) added in order to allow soldering of electrodes to the contact pads. We then deposited a 3 μm insulating oxide layer using plasma-enhanced chemical vapor deposition over the entire wafer area, except for a 10 mm long and 5 mm wide rectangular area exposing a short segment of the electrodes and serving as the actuation area. The third layer in the fabrication process was a mechanical support for the membrane's frame, determining the height of the Hele-Shaw chamber. We used SU8 photoresist to fabricate four 100 μm circular pillars with a diameter of 2 mm located at the four corners of the frame. The elastic sheet used in our device is made of low-density polyethylene (LDPE), which we first stretched manually over a large (14×10 cm) auxiliary frame. We then glued the pre-stretched sheet to the experimental frame (4×4 cm) and cut off the residual elastic sheet. Using Hooke's law we can obtain a rough estimation of the resulting tension. Under the assumption of isotropic pre-stretching, the

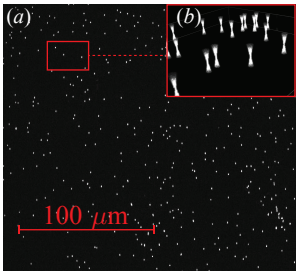

FIGURE S1. (a) Raw fluorescence image of the elastic sheet patterned with fluorescent microbeads. (b) During the sheet's deformation, at each time point we capture z stacks of images from which we obtain the three-dimensional point spread function (PSF) of the microbeads. The center of each PSF provides the location of bead associated with it.

tension $\tilde{T}$ scales linearly with the in-plane strain e_{strain}

$$\tilde{T} \sim \frac{\tilde{E}_{\text{Y}}\tilde{h}_{\text{m}}}{1-\nu} e_{\text{strain}}. \tag{A.1}$$

The Young's modulus of LDPE found in the literature is ~ 0.3 GPa, and thus for a 12 μm thick LDPE sheet, taking $\nu = 0.5$ and assuming that e_{strain} is $10^{-3} - 10^{-2}$, we obtain a rough estimation for tension as $\tilde{T} \sim 7200 e_{\text{strain}} = 7.2 - 72$ Pa m.

2. *Experimental procedure*

As shown in figure S1(a), we patterned the external side of the membrane by dehydrating an aqueous solution in an oven at a temperature of 85° C. We diluted a 0.5 ml aqueous solution consisting of deionized (DI) water and microbeads (initially containing 1 % solids, Fluoro-Max red fluorescent polymer microspheres, 2 μm diameter, Thermo Fisher Scientific, USA), at a ratio of 1:1500.

To fill the chamber with water, we first covered the electrodes with Kapton tape to protect them, and then used a corona-discharge wand (BD-20V, Electro-Technic Products, USA) on the glass substrate to improve the wetting, then placed 1 ml of deionized water (viscosity $\tilde{\mu} = 10^{-3}$ Pa s and permittivity $\tilde{\varepsilon} = 7.08 \cdot 10^{-10}\,\text{F m}^{-1}$) at the center of the chamber. We then placed the membrane (bounded by its rigid frame) on top of the pillars to create the microfluidic chamber. Finally, we connected the side electrodes to the output of a power source (Keithley 2230, Tektronix, USA), and the center electrode to its ground. We note that in our experiments the value of the zeta potential of the surfaces is not precisely known. While the zeta potential of the bottom glass substrate can be estimated approximately as -70 mV (Sze *et al.* 2003), the zeta potential of the LDPE elastic sheet is unknown, yet it is expected to be of $O(\pm 25$ mV), as this is the typical value found in the electrokinetic literature (Hunter 2000).

3. *Measurements and analysis*

To image the beads, we used a laser scanning confocal (LSM 510 META, Zeiss, Germany) connected to an upright motorized microscope (Axio Imager Z1, Zeiss, Germany), equipped with 20X 0.8 NA objective, and argon laser (488 nm) illumination. We focused on an area of 200 by 200 μm at the center of the membrane, where we expect to obtain maximum deformation. We then initiated a voltage of 15 V (resulting in an electric field of 3000 V m^{-1}) on the electrodes, and recorded vertical image stacks at a frame rate of 23 s between stacks, and 42 z-slices at a distance of 0.75 μm from one another within each stack, thus capturing the three-dimensional point spread function (PSF) of the beads,

as shown in figure S1(b). After 15 min we turned off the electric field, and continued imaging the membrane for an additional 15 min. To determine the location of the beads, we tracked the centers of the beads using the autoregressive mode in Imaris (Oxford Instruments, England). At every time point, we reported the average vertical positions of all the beads within the field of view, together with 95 % confidence bars based on Student's t-distribution for the mean value across 6 repeats.

B. Derivation of Green's functions solutions in rectangular domain

Sixth-order diffusion equations are encountered in various problems involving viscous–elastic interactions, such as viscous peeling (Hosoi & Mahadevan 2004), elastohydrodynamic wakes (Arutkin *et al.* 2017) and wrinkles (Kodio *et al.* 2017). However, to the best of our knowledge, the general solution of (2.13) with finite boundary conditions (2.15)–(2.16) in terms of Green's function has not been presented yet.

The Green's equation for the differential operator in (2.13) is given by

$$\frac{\partial g}{\partial t} - \lambda \nabla_{\parallel}^{6} g + \nabla_{\parallel}^{4} g = \delta(x-\xi)\delta(y-\eta)\delta(t), \tag{B.1}$$

subject to the boundary conditions (2.15)–(2.16) and the initial condition $g(x, y, t = 0) = 0$, where δ is Dirac's delta function.

We employ the finite sine transform with respect to x and y (Miles 1971),

$$G_{m,n}(t) \triangleq \int_0^{l_\mathrm{m}} \int_0^{w_\mathrm{m}} g(x, y, t) \sin\left(\frac{\pi m x}{l_\mathrm{m}}\right) \sin\left(\frac{\pi n y}{w_\mathrm{m}}\right) \mathrm{d}y\mathrm{d}x, \tag{B.2}$$

where the inverse transform is given as (Miles 1971)

$$g(x, y, t) \triangleq \frac{4}{l_\mathrm{m} w_\mathrm{m}} \sum_{m,\, n=1}^{\infty} G_{m,n}(t) \sin\left(\frac{\pi m x}{l_\mathrm{m}}\right) \sin\left(\frac{\pi n y}{w_\mathrm{m}}\right). \tag{B.3}$$

Applying the finite sine transform (B.2) on (B.1) and using (2.15)–(2.16) yields

$$\frac{dG_{m,n}(t)}{dt} + F(m, n; \lambda) G_{m,n}(t) = \sin\left(\frac{\pi m \xi}{l_\mathrm{m}}\right) \sin\left(\frac{\pi n \eta}{w_\mathrm{m}}\right) \delta(t), \tag{B.4}$$

where function $F(m, n; \lambda)$ is

$$F(m, n; \lambda) = \left(\left(\frac{\pi m}{l_\mathrm{m}}\right)^2 + \left(\frac{\pi n}{w_\mathrm{m}}\right)^2\right)^2 \left[\lambda \left(\left(\frac{\pi m}{l_\mathrm{m}}\right)^2 + \left(\frac{\pi n}{w_\mathrm{m}}\right)^2\right) + 1\right]. \tag{B.5}$$

Solving (B.4) together with initial condition $G_{m,n}(t = 0) = 0$, we obtain

$$G_{m,n}(t) = \sin\left(\frac{\pi m \xi}{l_\mathrm{m}}\right) \sin\left(\frac{\pi n \eta}{w_\mathrm{m}}\right) \mathrm{e}^{-F(m,n;\lambda)t}. \tag{B.6}$$

Substituting (B.6) into (B.3) provides the corresponding Green's function

$$g(x, y; \xi, \eta, t) = \frac{4}{l_\mathrm{m} w_\mathrm{m}} \sum_{m,\, n=1}^{\infty} \sin\left(\frac{\pi m \xi}{l_\mathrm{m}}\right) \sin\left(\frac{\pi n \eta}{w_\mathrm{m}}\right) \varphi(x, y, t; m, n), \tag{B.7}$$

where function $\varphi(x, y, t; m, n)$ is given by

$$\varphi(x, y, t; m, n) = \sin\left(\frac{\pi m x}{l_\mathrm{m}}\right) \sin\left(\frac{\pi n y}{w_\mathrm{m}}\right) \mathrm{e}^{-F(m,n;\lambda)t} = \chi(x, y; m, n) \mathrm{e}^{-F(m,n;\lambda)t}. \tag{B.8}$$

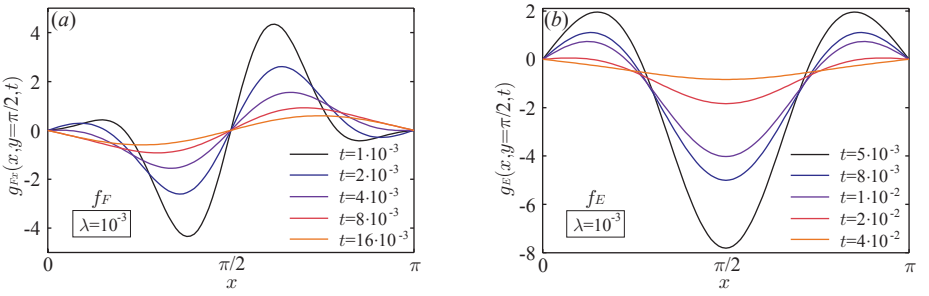

FIGURE S2. Green's-functions shapes along the $\hat{\boldsymbol{x}}$ axis for different times, describing the deformation due to a localized impulse (B.10) applied at the center of the configuration either (a) through the non-uniform slip velocity in the fluid or (b) through the pressure applied directly to the elastic sheet. All calculations were performed using $\lambda = 10^{-3}$ and $l_{\mathrm{m}} = w_{\mathrm{m}} = \pi$.

The deformation field is thus obtained by convolving the forcing with the Green's function (B.7), yielding

$$d(x,y,t) = \int_0^t \int_0^{l_{\mathrm{m}}} \int_0^{w_{\mathrm{m}}} \left(-\boldsymbol{\nabla}_{\xi,\eta} \cdot \boldsymbol{f}_F + \nabla^2_{\xi,\eta} f_E\right) g(x,y;\xi,\eta,t-\tau)\mathrm{d}\eta\mathrm{d}\xi\mathrm{d}\tau. \tag{B.9}$$

To provide more physical insight on the effect of driving forces on the resulting deformations, we further derive an explicit expression for the Green's functions resulting from the localized impulse

$$f_{F_x} = f_E = \delta(x-x_0)\delta(y-y_0)\delta(t), \tag{B.10}$$

acting either on the fluid or the elastic plate. Substituting (B.10) into (B.9) and using the identity $\int F(y)\delta^{(n)}(y-x)\,\mathrm{d}y = (-1)^n F^{(n)}(x)$ yields a general solution for the deformation field explicitly in terms of the external forces

$$d(x,y,t) = \int_0^t \int \left(\boldsymbol{f}_F(\xi,\eta,\tau)\cdot\boldsymbol{g}_F(x,y;\xi,\eta,t-\tau) + f_E(\xi,\eta,\tau)g_E(x,y;\xi,\eta,t-\tau)\right)\mathrm{d}\eta\mathrm{d}\xi\mathrm{d}\tau, \tag{B.11}$$

where $\boldsymbol{g}_F = \boldsymbol{\nabla}_{\xi,\eta} g$ and $g_E = \nabla^2_{\xi,\eta} g$. The expressions for $g_{F_x} = \boldsymbol{g}_F \cdot \hat{\boldsymbol{x}}$ and g_E read

$$g_{F_x} = \boldsymbol{\nabla}_{\xi,\eta}\cdot[g\hat{\boldsymbol{x}}] = \frac{4\pi}{l_{\mathrm{m}}^2 w_{\mathrm{m}}} \sum_{m,\,n=1}^{\infty} m\cos\left(\frac{\pi m\xi}{l_{\mathrm{m}}}\right)\sin\left(\frac{\pi n\eta}{w_{\mathrm{m}}}\right)\varphi(x,y,t;m,n), \tag{B.12}$$

$$g_E = -\frac{4\pi^2}{l_{\mathrm{m}}^3 w_{\mathrm{m}}^3} \sum_{m,\,n=1}^{\infty} \left(l_{\mathrm{m}}^2 n^2 + w_{\mathrm{m}}^2 m^2\right)\sin\left(\frac{\pi m\xi}{l_{\mathrm{m}}}\right)\sin\left(\frac{\pi n\eta}{w_{\mathrm{m}}}\right)\varphi(x,y,t;m,n). \tag{B.13}$$

For the purpose of illustration, in all of the following figures that are based on double series solutions, we truncate the series at $m = n = 100$. Figures S2(a) and S2(b) present the Green's functions (B.12) and (B.13), respectively, showing the deformations resulting from a localized impulse (B.10) applied at the center of the configuration, either through the non-uniform slip velocity in the $\hat{\boldsymbol{x}}$ direction or through the pressure applied directly to the elastic sheet in the $\hat{\boldsymbol{z}}$ direction.

C. Verification of analytical results presented in §§ 3-4

We performed dynamic numerical simulations to verify the analytical results obtained in §§ 3-4. Since in this study our main focus was on the tension-dominant regime, we set $\lambda = 0$ in the governing equation (2.14) and solved numerically the two-dimensional

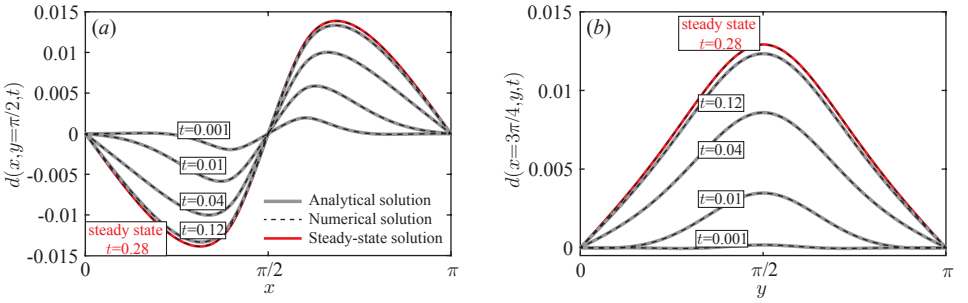

FIGURE S3. Comparison of numerical simulation results (dashed lines) and analytical solution (3.2) (solid lines) for the time-evolution of the deformation, resulting from a square-shape actuation f_{F_x} suddenly applied at the center of the configuration. (a) Time-evolution of the deformation profile along the $\hat{\boldsymbol{x}}$ axis for $y = \pi/2$. (b) Time-evolution of the deformation profile along the $\hat{\boldsymbol{y}}$ axis for $x = 3\pi/4$. Black dashed lines represent the numerical solution, while solid gray and red lines represent the time-dependent and steady-state analytical solutions, respectively. The numerical results are in very good agreement with the analytical solution. All calculations were performed using $l_{\mathrm{m}} = w_{\mathrm{m}} = \pi$, $c_x = c_y = \pi/2$ and $L = \pi/10$.

fourth-order evolution equation containing only the tension term,

$$\frac{\partial d}{\partial t} + \nabla_{\|}^4 d = -\boldsymbol{\nabla}_{\|} \cdot \boldsymbol{f}_F + \nabla_{\|}^2 f_E. \tag{C.1}$$

We first discretized spatial derivatives in (C.1) using a second-order central difference approximation with uniform grid spacing. Next, following Witelski & Bowen (2003) we implemented an alternating-direction-implicit (ADI) scheme, which employs operator splitting methods requiring the solution of two one-dimensional problems that result in considerable increase in efficiency. The resulting ADI scheme is unconditionally stable and first-order accurate in time due to the presence of mixed derivatives. In our simulations, we used 101×101 uniformly distributed grid points. Additionally, we performed grid sensitivity tests by increasing the number of grid points to 201×201 and 301×301, and established grid independence.

For illustration, in figure S3 we present the comparison of the analytical solution (solid lines) and numerically determined profile (dashed lines) for the deformation field, resulting from a square-shaped actuation, given by (3.1), suddenly applied at $t = 0$. The numerical results for the time-evolution of the deformation are in very good agreement with the analytical solution (3.2), as can be seen in figure S3 where the numerical and analytical solutions are almost indistinguishable for all times.

D. Asymptotic analysis for weak nonlinearity due to induced tension

We here derive the governing equations and the appropriate boundary conditions at the leading and first order, and provide closed-form solutions for the leading-order deformation and the first-order correction for the tension.

1. *Leading-order deformation field in an axisymmetric geometry*

At the leading order, tension is uniform and the deformation field is governed by a fourth-order diffusion equation containing a source term that depends on the driving forces with the corresponding boundary conditions

$$\frac{\partial d^{(0)}}{\partial t} + \nabla_r^4 d^{(0)} = -\boldsymbol{\nabla}_r \cdot \boldsymbol{f}_F + \nabla_r^2 f_E, \tag{D.1}$$

$$\frac{\partial d^{(0)}}{\partial r} = 0 \quad \text{and} \quad \lim_{r\to 0} r\frac{\partial}{\partial r}\left[\frac{1}{r}\frac{\partial}{\partial r}\left(r\frac{\partial d^{(0)}}{\partial r}\right)\right] = 0 \quad \text{at} \quad r = 0, \tag{D.2}$$

$$d^{(0)} = 0 \quad \text{and} \quad \frac{\partial}{\partial r}\left[r\frac{\partial d^{(0)}}{\partial r}\right] = 0 \quad \text{at} \quad r = R_{\mathrm{m}}. \tag{D.3}$$

We note that (D.1) is a counterpart of (C.1) in the limit $\lambda \to 0$, in an axisymmetric geometry. Similarly to section B, we can derive the general solution of (D.1)–(D.3) in terms of Green's functions. The corresponding Green's equation of (D.1) is

$$\frac{\partial g}{\partial t} + \frac{1}{r}\frac{\partial}{\partial r}\left[r\frac{\partial}{\partial r}\left[\frac{1}{r}\frac{\partial}{\partial r}\left[r\frac{\partial g}{\partial r}\right]\right]\right] = \frac{\delta(r-\xi)}{r}\delta(t), \tag{D.4}$$

subject to the boundary conditions (D.2)–(D.3) and the initial condition $g(r, \xi, t = 0) = 0$. To derive the solution for (D.4), we employ the finite Hankel transform with respect to r (Poularikas 2010)

$$G_n(t) \triangleq \int_0^{R_{\mathrm{m}}} r g(r,t) J_0\left(\frac{\chi_n r}{R_{\mathrm{m}}}\right) \mathrm{d}r, \tag{D.5}$$

where χ_n is the nth root of $J_0(\chi_n) = 0$ and the inverse transform is (Poularikas 2010)

$$g(r,t) \triangleq \frac{2}{R_{\mathrm{m}}^2}\sum_{n=1}^{\infty}\frac{G_n(t)}{J_1(\chi_n)^2} J_0\left(\frac{\chi_n r}{R_{\mathrm{m}}}\right). \tag{D.6}$$

Applying the finite Hankel transform (D.5) on (D.4) and using (D.2)–(D.3) yields

$$\frac{dG_n(t)}{dt} + \left(\frac{\chi_n}{R_{\mathrm{m}}}\right)^4 G_n(t) = J_0\left(\frac{\chi_n \xi}{R_{\mathrm{m}}}\right)\delta(t). \tag{D.7}$$

Solving (D.7) together with the initial condition $G_n(t = 0) = 0$, we obtain

$$G_n(t) = J_0\left(\frac{\chi_n \xi}{R_{\mathrm{m}}}\right)\exp\left(-\frac{\chi_n^4}{R_{\mathrm{m}}^4}t\right). \tag{D.8}$$

Substituting (D.8) into (D.6) yields the Green's function for the axisymmetric case

$$g(r;\xi,t) = \frac{2}{R_{\mathrm{m}}^2}\sum_{n=1}^{\infty}\frac{1}{J_1(\chi_n)^2} J_0\left(\frac{\chi_n \xi}{R_{\mathrm{m}}}\right) J_0\left(\frac{\chi_n r}{R_{\mathrm{m}}}\right)\exp\left(-\frac{\chi_n^4}{R_{\mathrm{m}}^4}t\right), \tag{D.9}$$

and the deformation field is obtained by convolving the forcing with the Green's function (D.9), resulting in

$$d^{(0)}(r,t) = \int_0^t \int_0^{R_{\mathrm{m}}} [-\boldsymbol{\nabla}_\xi \cdot \boldsymbol{f}_F(\xi,\tau) + \nabla_\xi^2 f_E(\xi,\tau)]\xi g(r;\xi,t-\tau)\mathrm{d}\xi\mathrm{d}\tau. \tag{D.10}$$

We further can express the resulting deformation field explicitly in terms of the driving forces

$$d^{(0)}(r,t) = \int_0^t \int_0^{R_{\mathrm{m}}} \xi[f_F(\xi,\tau) g_F(r;\xi,t-\tau) + f_E(\xi,\tau) g_E(r;\xi,t-\tau)]\mathrm{d}\xi\mathrm{d}\tau, \tag{D.11}$$

where g_F and g_E are the Green's functions resulting from the impulse force $f_F = f_E = \delta(r - r_0)\delta(t)/r$ applied at $r = r_0$,

$$g_F(r;\xi,t) = -\frac{2}{R_{\mathrm{m}}^3}\sum_{n=1}^{\infty}\frac{\chi_n}{J_1(\chi_n)^2} J_1\left(\frac{\chi_n \xi}{R_{\mathrm{m}}}\right) J_0\left(\frac{\chi_n r}{R_{\mathrm{m}}}\right)\exp\left(-\frac{\chi_n^4}{R_{\mathrm{m}}^4}t\right), \tag{D.12}$$

$$g_E(r;\xi,t) = -\frac{2}{R_{\rm m}^4}\sum_{n=1}^{\infty}\frac{\chi_n^2}{J_1\left(\chi_n\right)^2}J_0\left(\frac{\chi_n\xi}{R_{\rm m}}\right)J_0\left(\frac{\chi_n r}{R_{\rm m}}\right)\exp\left(-\frac{\chi_n^4}{R_{\rm m}^4}t\right). \tag{D.13}$$

2. *First-order correction for tension field in an axisymmetric geometry*

At the first order, $O(\alpha)$, the tension is spatially non-uniform and time-varying and is obtained through

$$\frac{1}{r}\frac{\partial}{\partial r}\left(r^3\frac{\partial T_r^{(1)}}{\partial r}\right) = -\frac{1}{2}\left(\frac{\partial d^{(0)}}{\partial r}\right)^2, \tag{D.14}$$

accompanied by the following boundary conditions

$$\frac{\partial T_r^{(1)}}{\partial r} = 0 \quad \text{at} \quad r = 0 \qquad \text{and} \qquad r\frac{\partial T_r^{(1)}}{\partial r} + (1-\nu)T_r^{(1)} = 0 \quad \text{at} \quad r = R_{\rm m}. \quad (D.15a,b)$$

The boundary condition (D.15b) implies that $T_r^{(1)}(r,t)$ does not contribute to the radial displacement at $r = R_{\rm m}$. Integrating (D.14) with respect to r and applying (D.15a) yields

$$\frac{\partial T_r^{(1)}}{\partial r} = -\frac{1}{2}\frac{1}{r^3}\int_0^r \xi\left(\frac{\partial d^{(0)}}{\partial \xi}\right)^2 \mathrm{d}\xi. \tag{D.16}$$

Integrating once again (D.16) and using (D.15b), we obtain a closed-form expression for the first-order correction of the tension

$$T_r^{(1)}(r,t) = T_r^{(1)}(R_{\rm m},t) + \frac{1}{2}\int_r^{R_{\rm m}}\frac{1}{\rho^3}\left[\int_0^{\rho}\xi\left(\frac{\partial d^{(0)}}{\partial \xi}\right)^2 \mathrm{d}\xi\right]\mathrm{d}\rho, \tag{D.17}$$

where

$$T_r^{(1)}(R_{\rm m},t) = \frac{1}{2(1-\nu)R_{\rm m}^2}\int_0^{R_m}\xi\left(\frac{\partial d^{(0)}}{\partial \xi}\right)^2 \mathrm{d}\xi. \tag{D.18}$$

Some physical insight on behavior of first-order correction can be obtained by inspecting (D.17) without requiring an exact solution. From (D.16) it follows that $T_r^{(1)}$ monotonically decreases for $r > 0$ and thus attains maximal value at the center of the membrane. Furthermore, since the integrands appearing in (D.17) and (D.18) as well as the integration interval are non-negative, the first-order tension field is also non-negative, implying that $T_r^{(1)}$ contributes to the increase of total tension and in turn to the decrease of the resulting deformation.

Secondly, due to the nonlinear quadratic term, appearing in (D.17), which corresponds to leading-order Gaussian curvature and involves in general an infinite series of Bessel functions, the double integration in calculating $T_r^{(1)}(r,t)$ usually seems to require numerical computations. However, in the case when the leading-order deformation can be expressed in terms of simple functions and the integrations in (D.17) can be performed, (D.17) provides the closed-form analytical solution for the tension correction.

3. *First-order correction for deformation field in an axisymmetric geometry*

The first-order deformation field is described by the inhomogeneous fourth-order diffusion equation

$$\frac{\partial d^{(1)}}{\partial t} + \nabla_r^4 d^{(1)} = -\nabla_r^2[\boldsymbol{\nabla}_r\cdot(T_r^{(1)}\boldsymbol{\nabla}_r d^{(0)})], \tag{D.19}$$

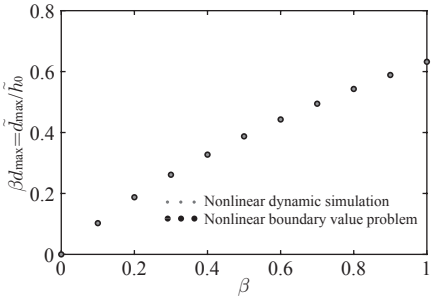

FIGURE S4. Cross validation of the two numerical methods, showing the scaled maximum deformation $\beta d_{\max} = \tilde{d}_{\max}/\tilde{h}_0$ as a function of the parameter β, for $\alpha = 0$. Black dots represent the solution of the state-state boundary value problem (6.4)–(6.5) and gray dots represent the state-state solution of the dynamic simulation. All calculations were performed using $V_r = -2$, $\nu = 0.5$ and $R_\mathrm{m} = 2$.

supplemented with the following boundary conditions

$$\frac{\partial d^{(1)}}{\partial r} = 0 \quad \text{and} \quad \lim_{r\to 0} r\frac{\partial}{\partial r}\left[\frac{1}{r}\frac{\partial}{\partial r}\left(r\left(\frac{\partial d^{(1)}}{\partial r} - T_r^{(1)}\frac{\partial d^{(0)}}{\partial r}\right)\right)\right] = 0 \quad \text{at} \quad r = 0, \tag{D.20}$$

$$d^{(1)} = 0 \quad \text{and} \quad \frac{\partial}{\partial r}\left[r\frac{\partial d^{(1)}}{\partial r}\right] = -\frac{\partial}{\partial r}\left[rT_r^{(1)}\frac{\partial d^{(0)}}{\partial r}\right] \quad \text{at} \quad r = R_\mathrm{m}. \tag{D.21}$$

We note that the source term in (D.19) arises from the internal tension formed in the elastic sheet due to the leading-order deformation. As opposed to leading-order deformation where the general solution can be readily determined using Green's functions (D.12) and (D.13), and despite the linearity, it is difficult to obtain a closed-form solution for (D.19), owing to the source term and the inhomogeneous boundary conditions, both involving multiplication of $d^{(0)}(r,t)$ and $T_r^{(1)}(r,t)$. We also note that for time-independent external forcing the steady-state deformation and tension distributions depend solely on the spatial coordinate and (D.19) can be greatly simplified to yield a closed-form expression for the first-order deformation field

$$d_\mathrm{s}^{(1)}(r) = \int_r^{R_\mathrm{m}} T_{r,\mathrm{s}}^{(1)}\frac{\mathrm{d}d_\mathrm{s}^{(0)}}{\mathrm{d}\xi}\mathrm{d}\xi, \tag{D.22}$$

where the subscript s denotes the steady state.

E. Details of numerical methods and their cross validation

The numerical results presented in § 6 were obtained using two numerical methods. In the first method, which was used to study the effect of hydrodynamic nonlinearity (h^3) on the transient behavior and the magnitude of deformation, we assumed the case of strong pre-stretching, i.e. $T_r = 1$, and solved numerically the nonlinear evolution equation (6.5). We first discretized spatial derivatives in (6.5) using a second-order central difference approximation with uniform grid spacing, leading to a series of ordinary differential equations for the evolution of $d_i(t) = d(r_i, t)$. We then integrated forward in time the resulting set of ordinary differential equations using MATLAB's routine `ode45`.

The second numerical method was employed to explore the effect of nonlinearity on the steady-state behavior, in which we solved numerically the corresponding steady-state boundary value problem (6.4)–(6.5) subject to the six boundary conditions (6.6)–(6.8) using MATLAB's routine `bvp4c`. We obtained the numerical solutions by beginning with

very small values of α and β, and using the leading-order asymptotic solution (6.12) for deformation and $T_r = 1$ for tension as initial guesses. Solutions for other values of α and β are then computed through numerical continuation.

We first validated our time-dependent (first method) and boundary value (second method) numerical solvers by comparison with the leading-order asymptotic solution (6.12) in figures 8(a) and 7(c), respectively, showing very good agreement. As an additional cross validation, figure S4 presents $\beta d_{\max}$ as a function of the parameter β, for $\alpha = 0$, determined from the two numerical methods, showing very good agreement between the results. Gray dots correspond to the value of $\beta d_{\max}$ obtained from the dynamic simulation at $t = 2.5$, where the system reached a steady state, as shown in figure 8(c), and black dots correspond to the results obtained from the state-state boundary value problem (6.4)–(6.5).

REFERENCES

Arutkin, M., Ledesma-Alonso, R., Salez, T. & Raphaël, E. 2017 Elastohydrodynamic wake and wave resistance. *J. Fluid Mech.* **829**, 538–550.

Hosoi, A. E. & Mahadevan, L. 2004 Peeling, healing, and bursting in a lubricated elastic sheet. *Phys. Rev. Lett.* **93** (13), 137802.

Hunter, R. J. 2000 *Foundations of colloid science*. Oxford University Press.

Kodio, O., Griffiths, I. M. & Vella, D. 2017 Lubricated wrinkles: Imposed constraints affect the dynamics of wrinkle coarsening. *Phys. Rev. Fluids* **2** (1), 014202.

Miles, J. W. 1971 *Integral transforms in applied mathematics*. Cambridge University Press.

Poularikas, A. D 2010 *Transforms and applications handbook*. CRC press.

Sze, A., Erickson, D., Ren, L. & Li, D. 2003 Zeta-potential measurement using the smoluchowski equation and the slope of the current–time relationship in electroosmotic flow. *J. Colloid Interface Sci.* **261** (2), 402–410.

Witelski, T. P. & Bowen, M. 2003 ADI schemes for higher-order nonlinear diffusion equations. *Appl. Numer. Maths* **45** (2-3), 331–351.